Applications in Engineering Science 15 (2023) 100131

Contents lists available at ScienceDirect

Applications in Engineering Science

journal homepage: www.elsevier.com/locate/apples

Analysis and modeling of the strain distribution and evolution during a fatigue test in ULCF and LCF on a friction stir welded specimen from steel and aluminum

Paul Dario Toasa Caiza [a,*], Yoshihiko Uematsu [b]

[a] KIT Stahl- und Leichtbau, Versuchsanstalt für Stahl, Holz und Steine, Karlsruher Institut für Technologie (KIT), Otto-Ammann-Platz 1, 76131 Karlsruhe, Germany
[b] Department of Mechanical Engineering, Gifu University, 1-1 Yanagido, Gifu 501-1193, Japan

ARTICLE INFO

Keywords:
Strain
Cyclic loading
Gaussian model
Lifetime estimation
DIC

ABSTRACT

Under cyclic loading in ULCF and LCF regimes the strain plays a fundamental role in the analysis of the fatigue resistance and in the estimation of the fatigue life. The DIC method, which allows to acquire strain and deformation in large areas is applied in order to obtain the maximum reached strain, strain range, mean strain and SWT parameter during a fatigue test on a friction stir welded specimen. Since the distribution of these variables in the region of interest shows a geometry given by a symmetric bell, a Gaussian model is considered to model it. The evolution of these variables during the fatigue test up to failure is fitted by applying a third grade polynomial. The obtained results, show the plausibility of the proposed method to model the strain distribution and evolution under cyclic loading.

1. Introduction

Nowadays, the use of components manufactured by joining dissimilar alloys, such aluminum and steel plays an important role in the automotive and aerospace industry. The friction stir welding (FSW) method (Kumar et al., 2015; Watanabe et al., 2006; Hatano et al., 2018; Wang et al., 2019; Matsuda et al., 2020; Liu and Dong, 2021) is one alternative to join aluminum (Al) alloy and steel plates, which afterwards are used to manufacture the components required by the industries mentioned above. The analysis and estimation of the fatigue strength of these components is a mandatory task, since their safety and reliability have to be guaranteed. This task can be accomplished by evaluating experimental data obtained from fatigue experiments (Okane et al., 2017; Uematsu et al., 2020; Sandnes et al., 2022). Particularly, the fatigue strength in ultra low cyclic fatigue (ULCF) and low cycle fatigue (LCF) regimes depends strongly on the strain. Usually, strain gauges are used to measure the strain during fatigue tests. However, these gauge allow only a local measure of the strain. Another option is the application of the Digital Image Correlation (DIC) method, see Chambers (2017), Uematsu et al. (2021). The DIC method offers the possibility of capturing strain, displacement and deformation in large areas with higher accuracy. This fact represents the main advantage of DIC in comparison with using strain gauges, which measure the strain in discrete and finite locations, see Górszczyk et al. (2019). Additional advantage of the DIC method are well described in Abdulqader and Rizos (2020).

2. Fatigue experiments

2.1. Materials and welding conditions

The materials used to manufacture the specimen are Al alloy, A6061-T6, and stainless steel, type 304, plates with the width of 75 mm and length of 150 mm. The thicknesses of A6061 and type 304 plates are 6 and 5 mm, respectively. The Friction Stir Welding (FSW) tool with concave shoulder, with a diameter of 14 mm, was used for the joining, see Fig. 1. The tool has a threaded probe with the diameter of 6 mm and length of 4.7 mm, see Fig. 2. The tool rotational and traveling speeds were fixed at 700 rpm and 100 mm/min, respectively. The tool plunge depth and tool-to-work piece angle were 0.8 mm and 3° from the vertical axis, respectively. The detailed joining procedures and microstructures in the stir zone (SZ) are described in our previous study, see Ogawa et al. (2019).

2.2. Experimental procedures

In the as-welded plate, 0.1 mm from the top surface and 0.9 mm from the bottom surface were removed by milling as schematically shown in Fig. 3.

Subsequently, the tensile specimens were sampled from the welded plates by electrical discharge machining. Tensile tests were conducted

* Corresponding author.
E-mail address: paul.toasa@kit.edu (P.D. Toasa Caiza).

https://doi.org/10.1016/j.apples.2023.100131
Received 5 January 2023; Accepted 31 March 2023
Available online 11 April 2023

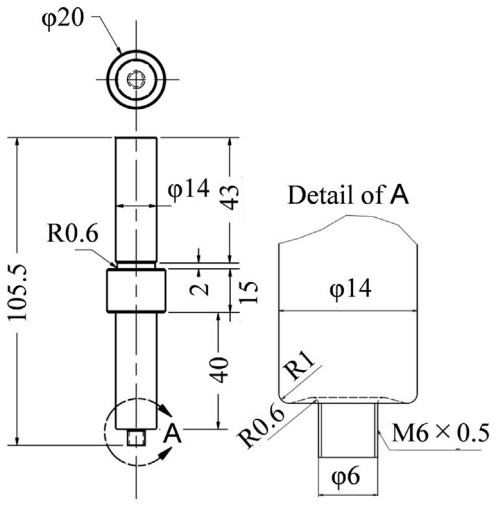

Fig. 1. Geometry of the FSW tool.

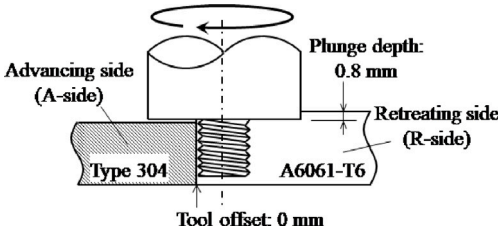

Fig. 2. Schematic illustration of joining process.

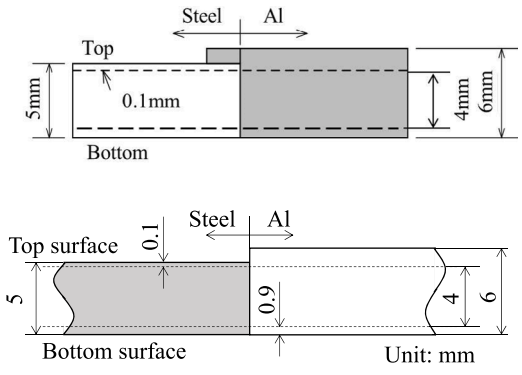

Fig. 3. Schematic illustration showing the surface removal process.

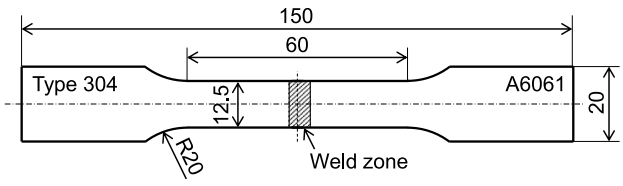

Fig. 4. Geometry of the specimen subjected the tensile tests.

using the specimens in accordance with JIS (Japanese Industrial Standard) Z 2241 13B, where the test piece has the gauge length of 50 mm and the width of 12.5 mm as shown in Fig. 4.

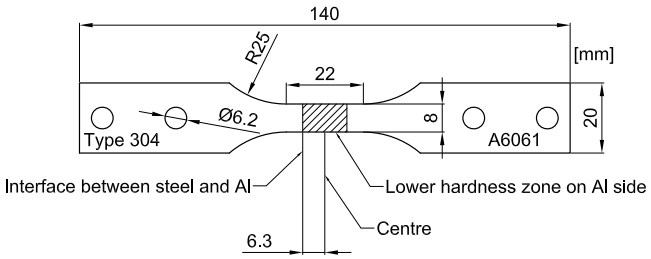

Fig. 5. Geometry of the specimen subjected to the fatigue tests.

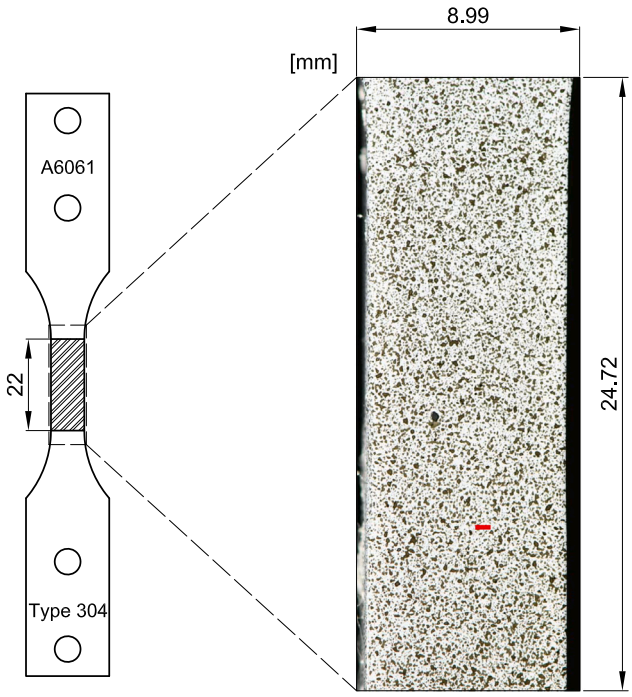

Fig. 6. ROI considered to perform the DIC method.

The tool center corresponds to the center of the gauge length of the tensile specimen. Tensile tests were conducted using an electro-hydraulic testing machine (SHIMADZU: EHF-LV-020k1-020).

The geometry of the specimens used in the fatigue experiments is shown in Fig. 5.

A digital camera, Nikon D7500, with the CMOS sensor with the size of 23.5 × 15.7 mm was used to acquire the images of the surface under study, which is also know as Region of Interest (ROI). The lens of the digital camera was Nikon AF-S VR Micro-Nikkor 105 mm f/2.8G IF-FD. Random dot patterns on the ROI were formed by white and black color sprays. In the DIC procedure, deformation is measured by the matching of luminance distribution in the ROI before and after loading. The location and appearance of the ROI considered in this study are shown in Fig. 6.

2.3. Hardness distribution

The detailed microstructures and mechanical properties are described in Ogawa et al. (2018) and Ogawa et al. (2019),so that, the hardness distribution is briefly described in this section. The lower

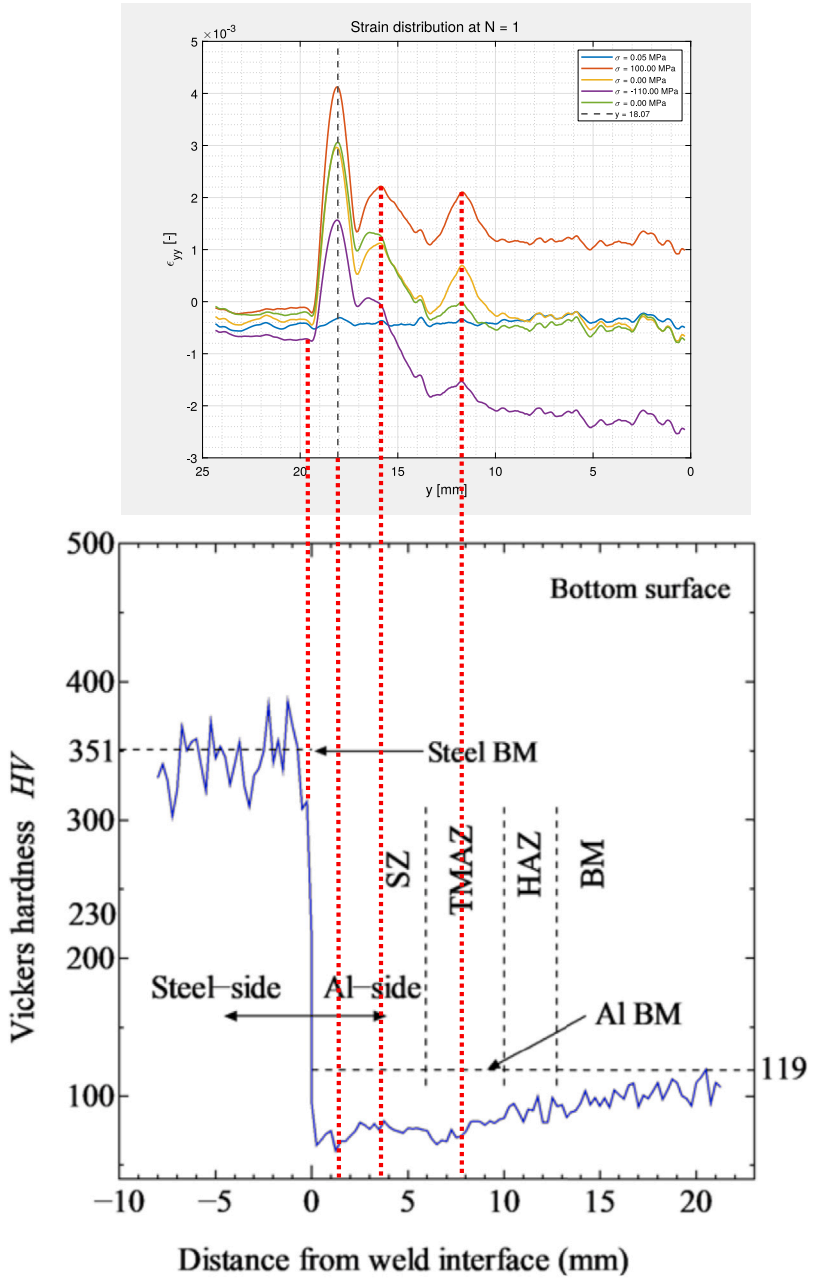

Fig. 7. Hardness distribution on the bottom side.

graphic on Fig. 7 shows the Vickers hardness profile on the bottom surfaces of the specimens.

Softening occurred in the SZ due to the heat input during FSW, and the minimum hardness appeared at the thermo-mechanically affected zone (TMAZ). It should be noted that the minimum hardness appears at about 9 mm away from the interface on the top surface, whilst and about 6.5 mm on the bottom surface. In addition, the hardness near the interface (0 1 mm) on the bottom surface was nearly comparable to the minimum hardness at 6.5 mm away from the interface. The hardness mapping measured on the Al side surface is shown in Fig. 8 (Ogawa et al., 2019). It should be noted that the area of lower hardness (blue area) in the TMAZ has vertical asymmetricity, where lower hardness appears further from the interface on the top side. Furthermore, minimum hardness appears near the interface (0 3 mm) only on the bottom side.

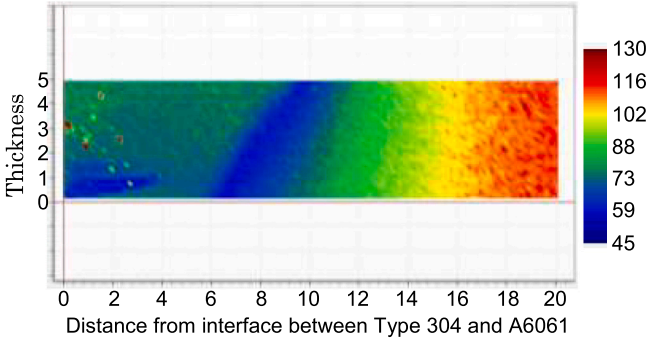

Fig. 8. Hardness mapping measure on the Aluminum side surface.

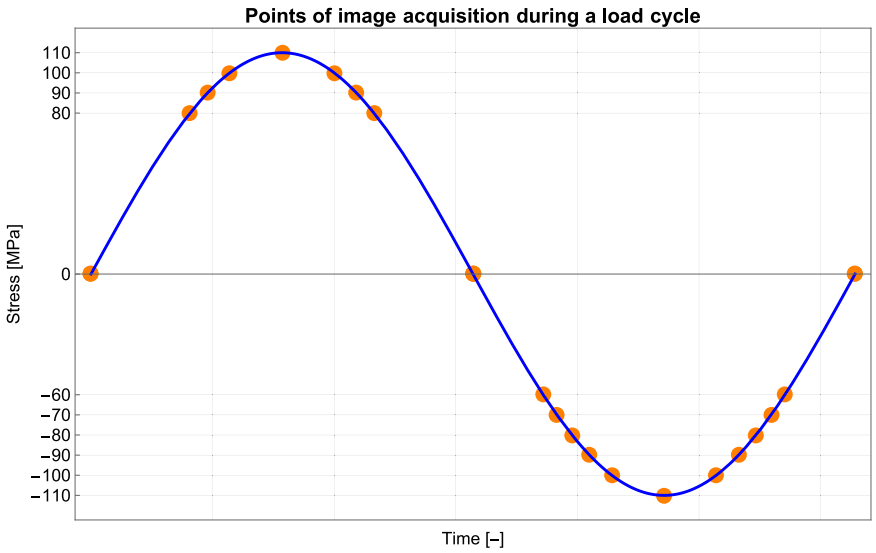

Fig. 9. Stress values corresponding to the digital image acquisition during a loading cycle.

Table 1
Stress values corresponding to the digital image acquisition during a loading cycle.

	Increasing	Decreasing
Tension [MPa]	0, 0.05, 80, 90, 100, 110	100, 90, 80, 0.05,0
Compression [MPa]	−0,05, −60, −70, −80, −90, −100, −110	−100, −90, −80, −70, −60, −0.05, 0

3. DIC method applied on the bottom side

3.1. Image acquisition

The fatigue experiment was performed under a stress range of 220 MPa and a stress ratio $R = -1$. The fatigue failure occurred at the loading cycle $N = 6461$.

According to the procedure described in Section 2.2, twenty five digital images were taken at fifteen cycles. The specific moments when the images were taken during a loading cycle are shown in Fig. 9 and described in Table 1.

3.2. Application of the DIC method

For every cycle, in which the digital pictures were taken, the DIC method was applied to calculate the strain and to display its distribution. Since there are 375 pictures of the strain distribution, as example only the pictures corresponding to the cycles $N = 5$ and $N = 3000$ are shown in Figs. 10 and 11.

Once the strain distribution has been obtained, it is possible to obtain several variables or parameters, which depend on the strain and on the loading cycle.

3.2.1. Maximum strain location

The first results obtained after applying the DIC method are the maximum strain values and their location as they are shown in Table 2. According to the dimensions of the images taken during the experiment, the points where the maximum strain is reached are located in the red region that is marked in Fig. 12.

Thus, the maximum strain is reached within a tight region, located around 18 mm from the top of the ROI. As a matter of fact, the strain distribution has a bell geometry, which starts at the interface of steel and aluminum and reaches its peak on the SZ, see upper graphic on Fig. 7. There are two more lower peaks on the strain distribution, they are located on the SZ and on the TMAZ.

In the x direction the maximum strain is reached in a brighter region, however its size and location are not relevant since the loading during the fatigue test is along the y axis.

Table 2
Location and value of the maximum strain reached during the fatigue test up to failure at $N = 6461$.

N [–]	Max. Strain [–]	X-coord [mm]	Y-coord [mm]
1	0.0041231447	5.03	18.07
2	0.0052560423	4.96	18.07
3	0.0056512649	4.81	18.07
4	0.0058712825	5.11	18.07
5	0.0058829590	4.81	18.15
6	0.0060677354	5.25	18.07
7	0.0062312116	4.81	18.07
8	0.0062877001	4.96	18.07
9	0.0061845778	4.96	18.15
10	0.0062264002	4.96	18.15
100	0.0066539869	5.11	18.07
500	0.0072175299	5.03	18.15
1000	0.0076959070	5.03	18.15
3000	0.0088001000	5.33	18.07
5000	0.0126490250	5.33	18.07
6461	0.0131306	–	–

4. Modeling of strain distribution and evolution

As it was mentioned before, after performing the DIC method on the digital images, the distribution and evolution of the strain and other related variables on the region showed in Fig. 12 can be obtained, see Figs. 10 and 11.

4.1. Strain distribution

Since of particular interest are the points where the maximum strain is reached, it is possible to plot the strain distribution through these points and along the x and y axis. A particular example is shown in Fig. 13, which displays the strain distribution during the loading cycle $N = 1$ under five different stresses at the point (5.03, 18.07) mm. The strain distribution along the x axis does not vary too much in each stage. However, along the y axis the strain has a very particular geometry, given by a bell, whose highest point is located where the

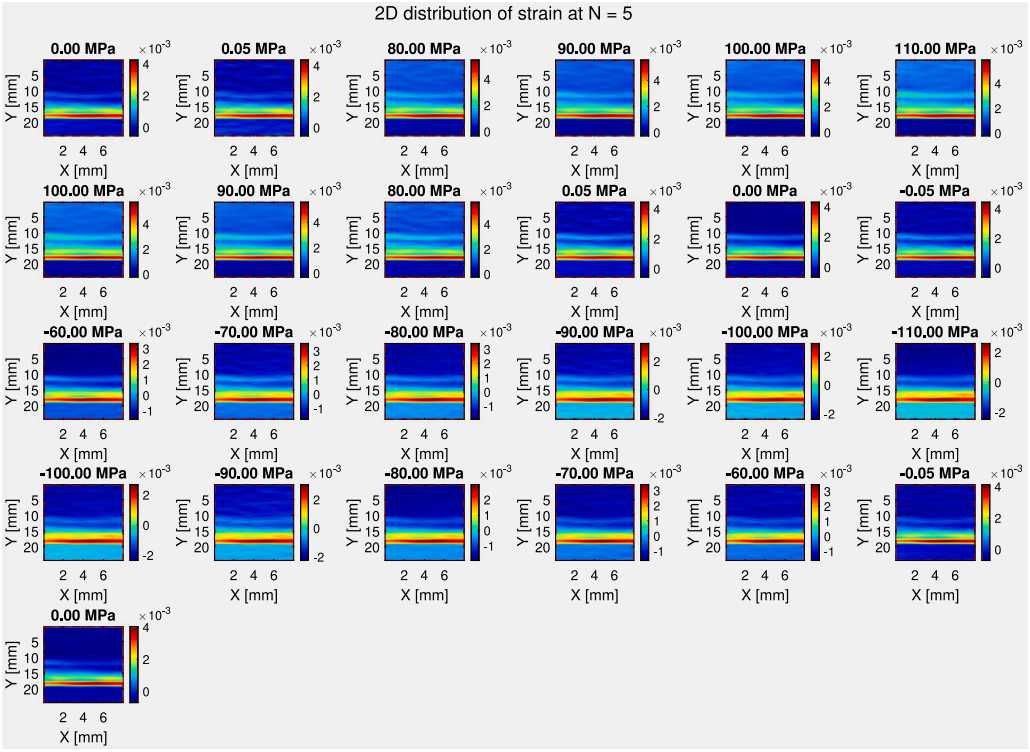

Fig. 10. Strain distribution during the loading cycle $N = 5$.

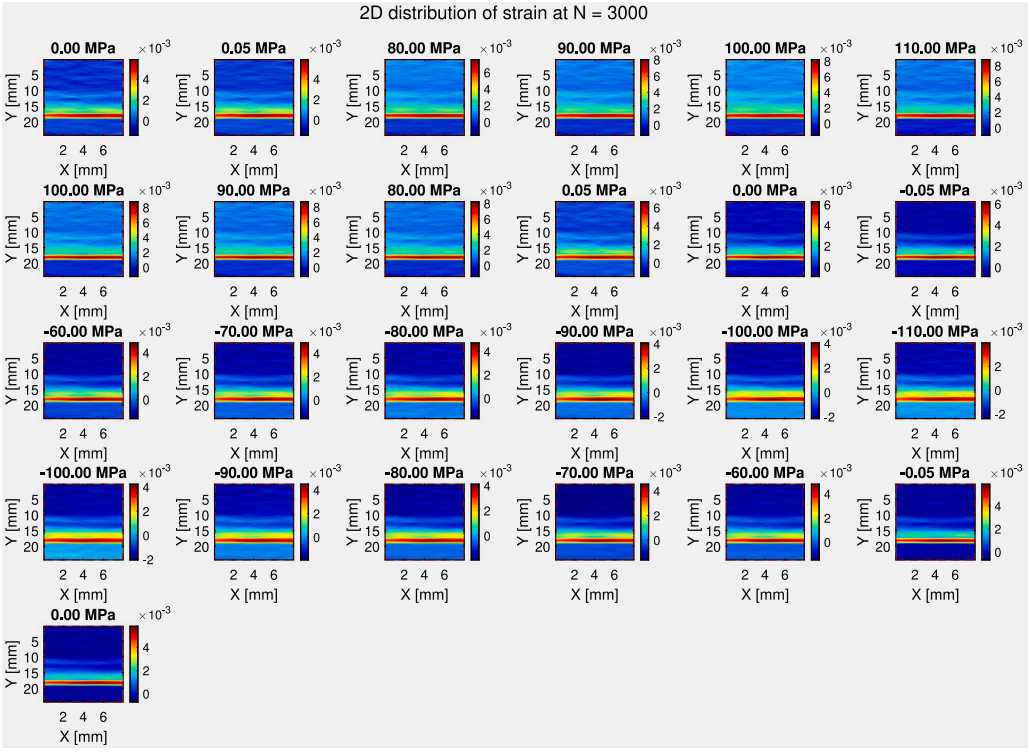

Fig. 11. Strain distribution during the loading cycle $N = 3000$.

maximum strain for a given stress is reached. Moreover, on the left side corresponding to Aluminum there are two additional small bells, while on the right side corresponding to the Steel the variation of the strain is much smaller.

Since the maximum strain is reached under tension, it is important to see how the strain changed during the fatigue test. The Fig. 14 shows the maximum strain reached during the fatigue test, along the loading axis y and at $x = 5.03$ mm. The corresponding loading cycles and strain

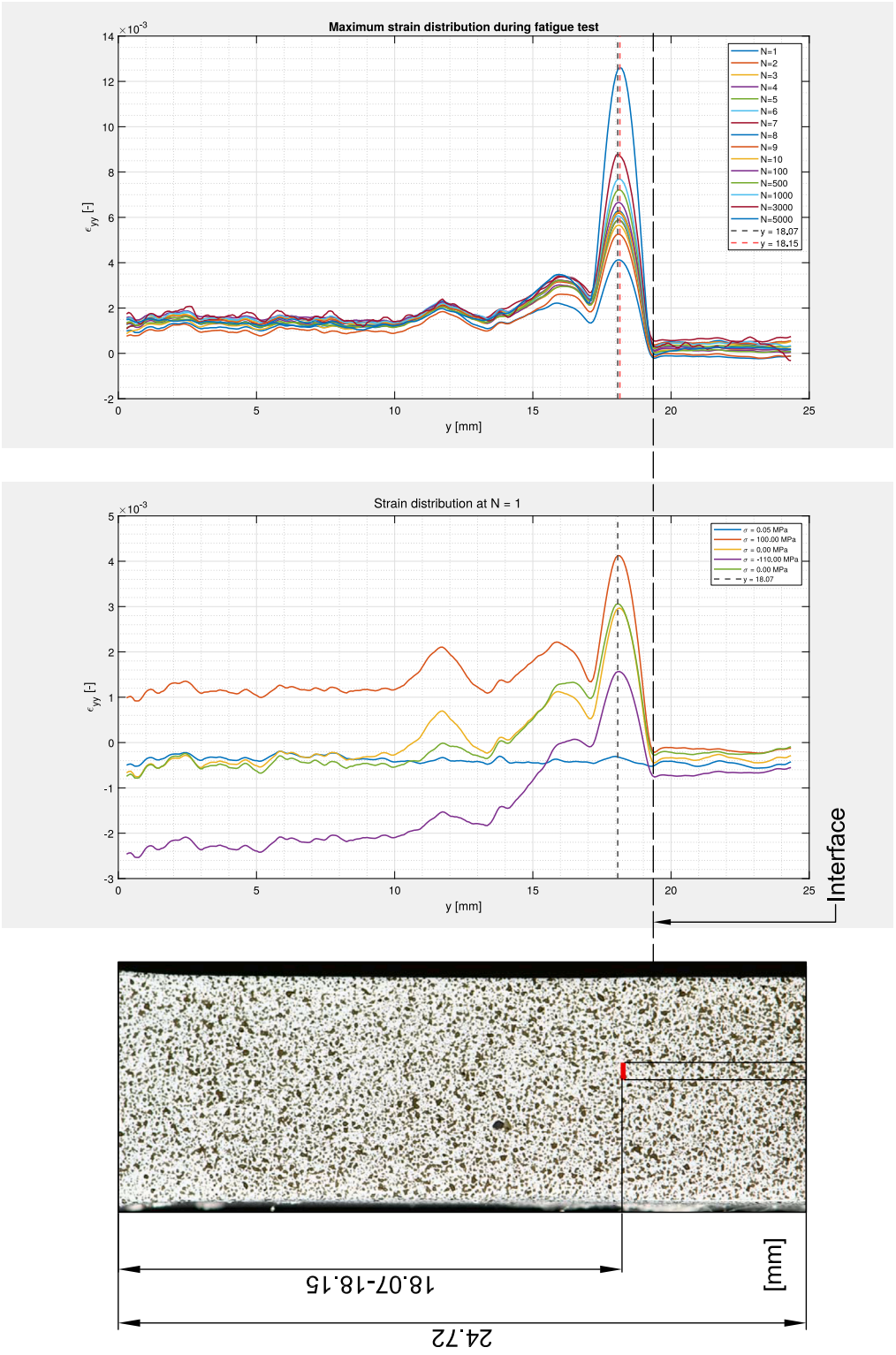

Fig. 12. Region where the maximum strain is reached. Position compared with the data of the first loading cycle and of the complete fatigue experiment.

values are those shown in Table 2. During all fatigue test the strain distribution kept a bell geometry, which is symmetric regarding the point where the maximum strain is reached. Moreover, the width on the basis of the bell keeps constant around 1 mm on each side. This symmetric behavior of the strain and its evolution up to failure suggests two approaches to evaluate these facts. On the one hand the strain geometric distribution could be modeled by applying a Gauss function. On the other hand the strain evolution could be modeled by applying power functions.

4.2. Gaussian modeling of the maximum strain distribution

The preliminary results show that the strain during the fatigue test has a particular geometry given by a bell along the load direction y, see Fig. 14. The highest strain values are located at the peak of the bell,

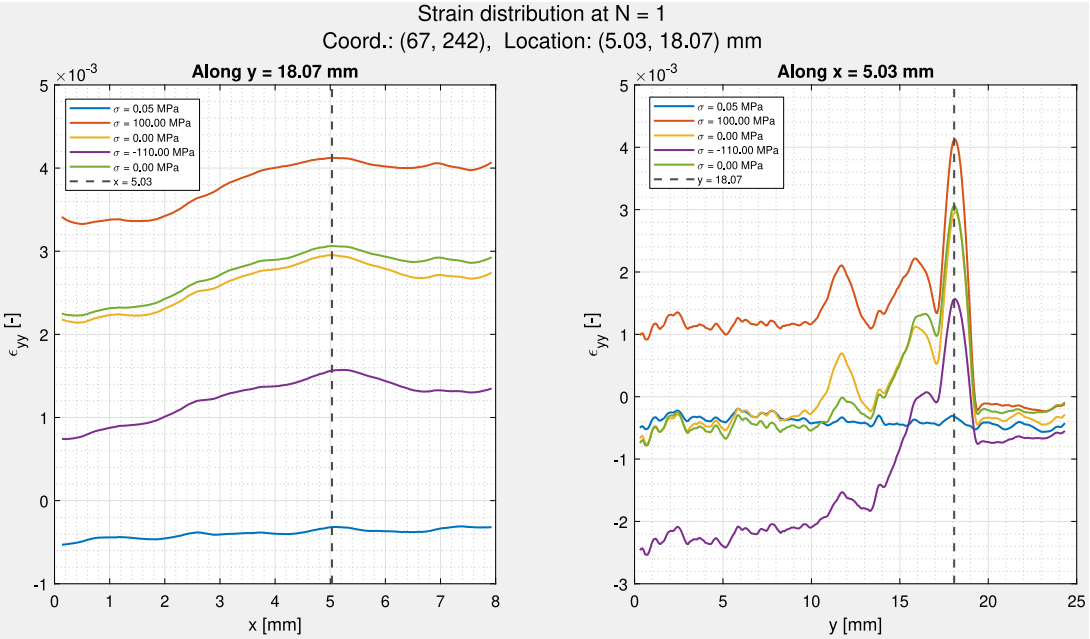

Fig. 13. Strain distribution across the point (5.03, 18.07) mm, where the maximum strain is reached during the loading cycle $N = 1$.

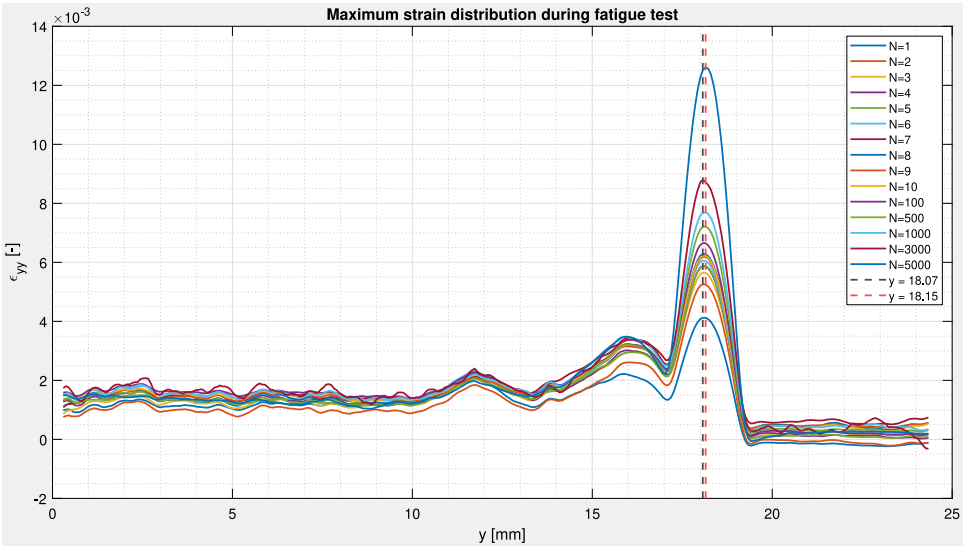

Fig. 14. Maximum strain distribution during the fatigue test along the loading axis y and $x = 5.03$ mm.

which matches with the SZ that indeed has the lowest hardness value, see Fig. 7. There are two additional lower peaks, which are located in the SZ and in the TMAZ.

According to these results, it seems plausible that the strain distribution along the loading axis y can be described by a Gaussian model.

A Gauss function $G(a, b, c)$ is a symmetric curve in form of bell given by

$$f(x) = a \cdot e^{-\left(\frac{x-b}{c}\right)^2}, \qquad a, b \in \mathbb{R}, c > 0 \tag{1}$$

where a is the height or maximum value of the curve, b is the position of the peak or center of the curve and c is related the width of the bell, see Fig. 15.

Particularly, the parameter c is related with the width of the bell at the half of its maximum, which is known as full width at half maximum (FWHM) and it is given by

$$FWHM = 2\sqrt{\log(2)}c \tag{2}$$

Among its applications, the Gauss function is used to model peaks of functions by considering a Gaussian mode given by

$$y = \sum_{i=1}^{n} a_i \cdot e^{-\left(\frac{x-b_i}{c_i}\right)^2}, \tag{3}$$

where n is the number of peaks to fit.

Thus, it seems plausible to apply a Gaussian model to fit the strain along the loading axis y. Then, as it has been shown in Fig. 14, the geometrical distribution of the strain along the tension axis y can be described by the sum of three Gauss functions.

An example of three Gaussian functions consider to model the strain distribution are shown in Fig. 16.

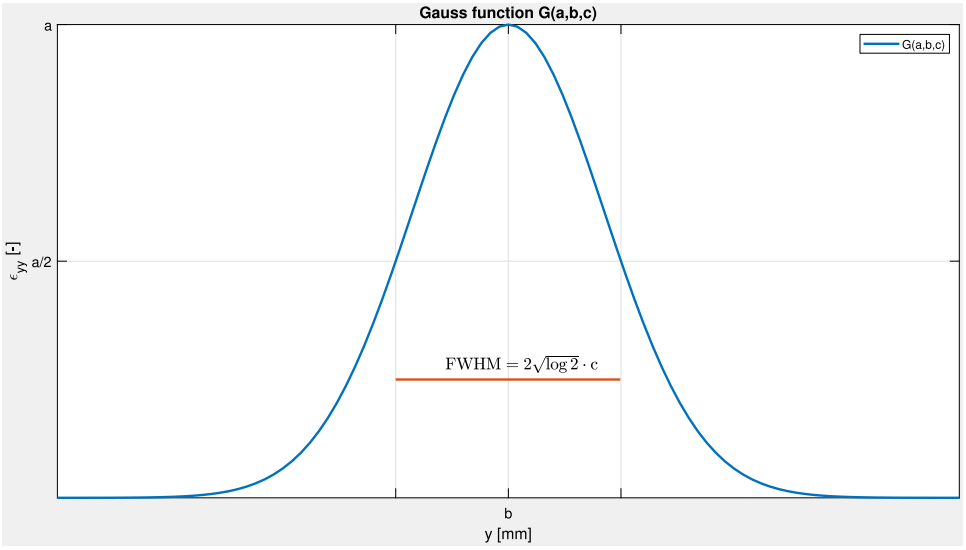

Fig. 15. Typical Gauss function.

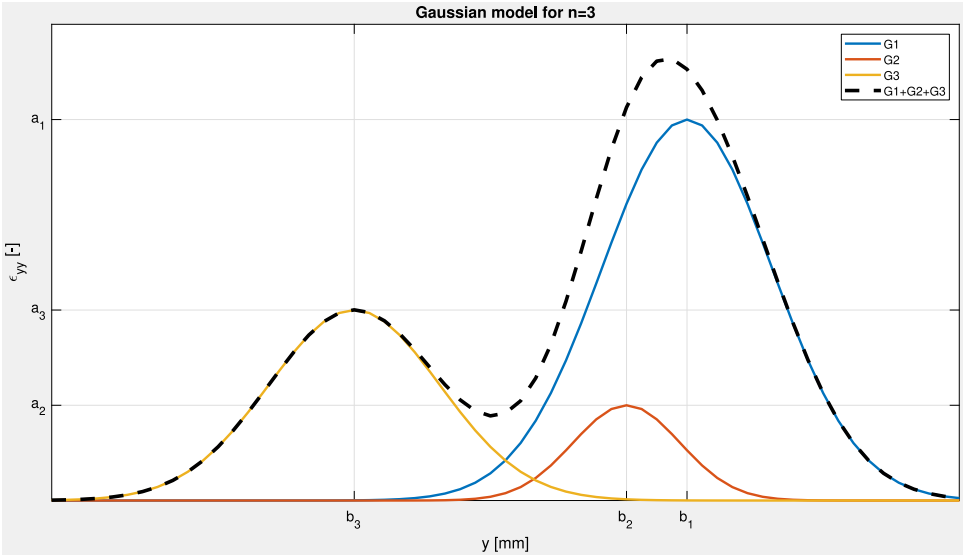

Fig. 16. Sum of three Gauss functions.

Taking into consideration the experimental data, the modeling of the strain based on a Gaussian model was performed. The Fig. 17 shows the fitting the curves for every loading cycle during the fatigue test.

The estimation of the parameters corresponding to the Gaussian model are shown in Table 3.

4.3. Modeling of the maximum strain evolution

According to the experimental results, the maximum strain increases during the fatigue test, see Table 2. This strain variation can be modeled as well. In this case, a polynomial of grade 3 given by

$$\log(\epsilon_{yy}) = a_0 + a_1(\log N) + a_2(\log N)^2 + a_3(\log N)^3 \tag{4}$$

has been considered to do this. The polynomial parameters are shown in Table 4 and the fitting in Fig. 18.

4.4. Strain range distribution and evolution

From the results obtained by applying the DIC method it is also possible to evaluate the strain range evolution in the ROI. The Figs. 19 and 20 show the strain range distribution at the loading cycles $N = 1$ and $N = 3000$. At the beginning of the experiment, the variation of the strain range presents two peaks along the loading axis y. One small

Table 3
Parameter estimation of the Gaussian model.

N	a_1	b_1	c_1	a_2	b_2	c_2	a_3	b_3	c_3
1	0.004	18.183	0.683	0.000	18.002	0.268	0.002	15.689	1.966
2	0.004	17.994	0.539	0.003	18.623	0.389	0.003	15.963	1.983
3	0.005	18.157	0.702	0.001	18.618	0.319	0.003	15.886	2.130
4	0.005	18.168	0.701	0.001	18.658	0.307	0.003	15.903	2.102
5	0.023	18.788	0.935	0.003	15.897	2.382	−0.021	18.915	0.862
6	0.005	18.183	0.710	0.000	18.609	0.291	0.003	15.940	2.221
7	−0.002	18.188	0.380	0.007	18.188	0.619	0.003	16.013	2.743
8	0.005	18.207	0.694	0.000	18.447	0.000	0.003	15.971	2.398
9	0.005	18.210	0.707	0.003	15.975	2.459	0.000	18.059	0.000
10	0.006	18.262	0.755	0.008	22.386	6.925	−0.007	19.563	2.200
100	0.016	18.216	0.804	−0.011	18.218	0.913	0.003	16.222	2.464
500	0.006	18.323	0.610	0.002	17.697	0.370	0.003	15.973	2.186
1000	0.000	18.448	0.005	0.003	15.836	2.122	0.007	18.209	0.735
3000	0.000	18.148	0.012	0.008	18.202	0.709	0.003	15.980	2.175
5000	0.010	17.901	0.509	0.008	18.545	0.463	0.003	15.774	1.844

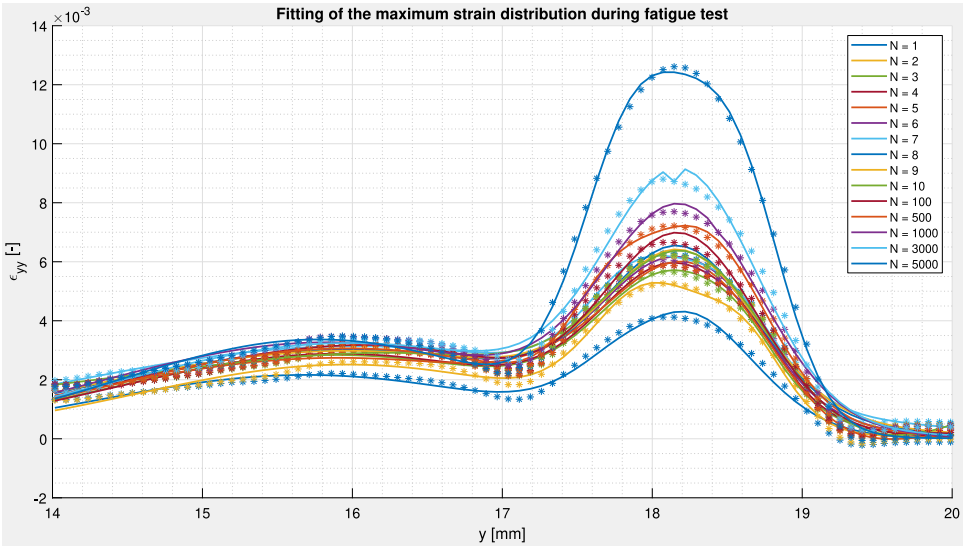

Fig. 17. Gaussian modeling of the maximum strain distribution along the loading axis y during the fatigue experiment.

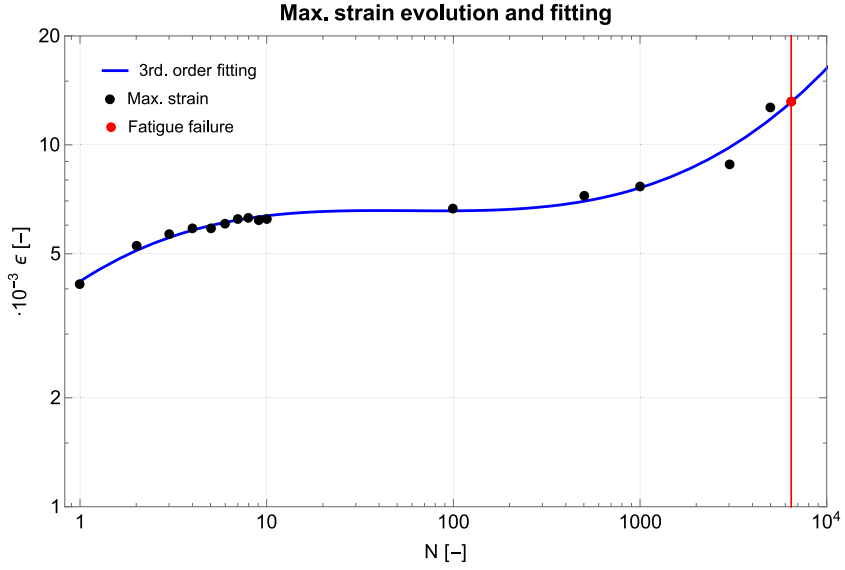

Fig. 18. Evolution of the maximum strain during the fatigue test up to failure at $N = 6461$.

Table 4
Strain evolution. Parameters of the fitting polynomial.

a_0	a_1	a_2	a_3
1.43395	0.33726	−0.0834764	0.00682264

peak at 11.21 mm and the big one at 18.15 mm on the loading axis. The location of the big peak matches with location of the point where the maximum strain is reached. However, as the experiment continues, only the big peak located in this region remains and increases. This behavior can be observed in Fig. 21, which shows the strain range evolution along the loading axis y at the point $x = 5.03$ mm during the fatigue test.

Particularly, at the loading cycle $N = 5000$, the peak of the strain range bell increased notably and its bottom decreased significantly. This behavior is expected, since the fatigue crack growths along the interface between steel and Al. Moreover, as it is known, the fatigue crack growth rates are faster in the final stage of fatigue failure.

It is very interesting to observe, that on the aluminum side, the stress range increases the farther from the TMAZ zone it is, and on the steel side the variation of the strain range is very small. Along the x axis, the strain range does not vary much, see Figs. 19 and 20.

Table 5
Location and value of the maximum strain range reached during the fatigue test up to failure at $N = 6461$.

N [-]	Strain range [-]	X coord [mm]	Y-coord [mm]
1	0.0039436403	0.13	11.21
2	0.0041038308	0.13	0.45
3	0.0041574483	0.13	0.3
4	0.0036198851	0.13	0.82
5	0.0040474463	0.13	1.7
6	0.0036216571	1.54	0.3
7	0.0041377258	0.13	0.45
8	0.0041267668	0.13	0.3
9	0.0038223939	1.02	0.3
10	0.0040355676	0.13	0.45
100	0.0039552718	0.13	0.3
500	0.0041553457	0.13	0.3
1000	0.0041759498	0.13	18.15
3000	0.0050337479	0.13	18.15
5000	0.009471433	0.13	0.37
6461	0.00908209		

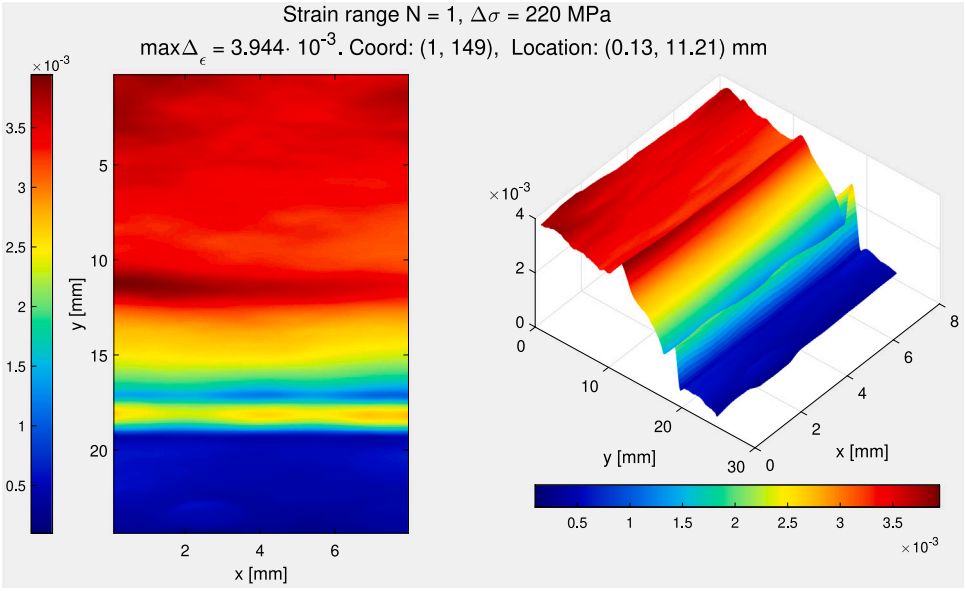

Fig. 19. Strain range distribution at the loading cycle $N = 1$.

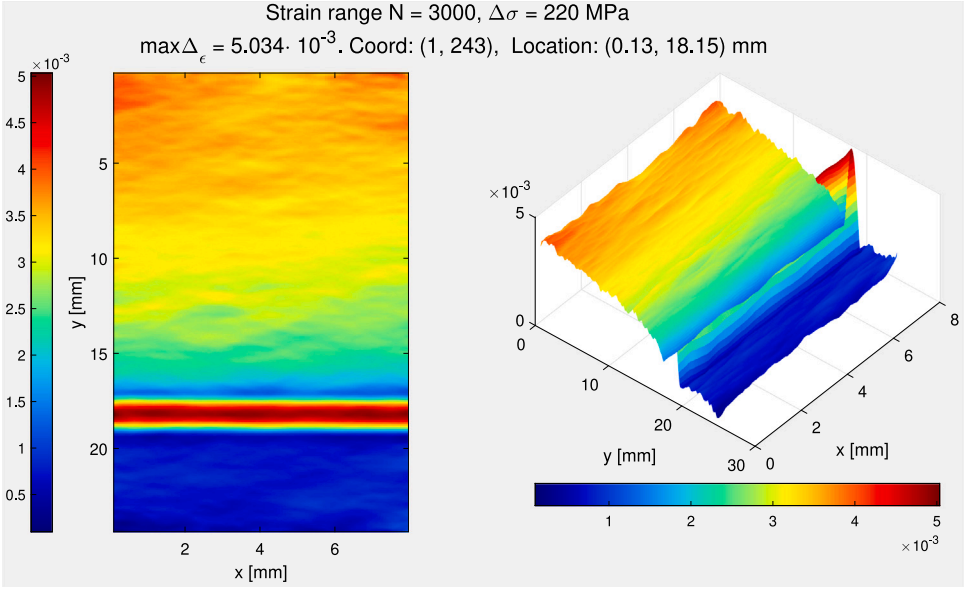

Fig. 20. Strain range distribution at the loading cycle $N = 3000$.

Table 6
Strain range evolution. Parameters of the fitting polynomial.

a_0	a_1	a_2	a_3
1.3362	0.107559	−0.0543424	0.00608497

Similar to the case of the maximum strain, the maximum strain range shown in Table 5 can be fitted by a third grade polynomial. The Table 6 shows the fitting parameters and Fig. 22 shows its fitting.

As it has been seen, the strain range distribution presents a bell geometry on the TMAZ and its main peak is located in the same region where the maximum strain is reached. Thus, this distribution could be also modeled by applying a Gaussian model and its evolution by a polynomial of third grade.

4.5. Mean strain distribution and evolution

It is well know that the mean strain plays an important role in the fatigue life of a structure, so that, observing how the mean strain varies under cyclic loading could provide additional information about the fatigue resistance of the specimen.

The Figs. 23 and 24 show the mean strain distribution corresponding to the loading cycles $N = 1$ and $N = 3000$. In this case, the maximum mean strain is reached on the same region where the maximum strain is observed, see Tables 2 and 7.

Like the maximum strain reached during the maximal tension and displayed on Fig. 14, the mean strain distribution along the loading axis y show three peaks with a bell geometry at the points $y = 11.73, 16.08, 18.15$ mm, see Fig. 25. On the one hand, at the left of the bell the mean stress varies while the test continues. On the other hand,

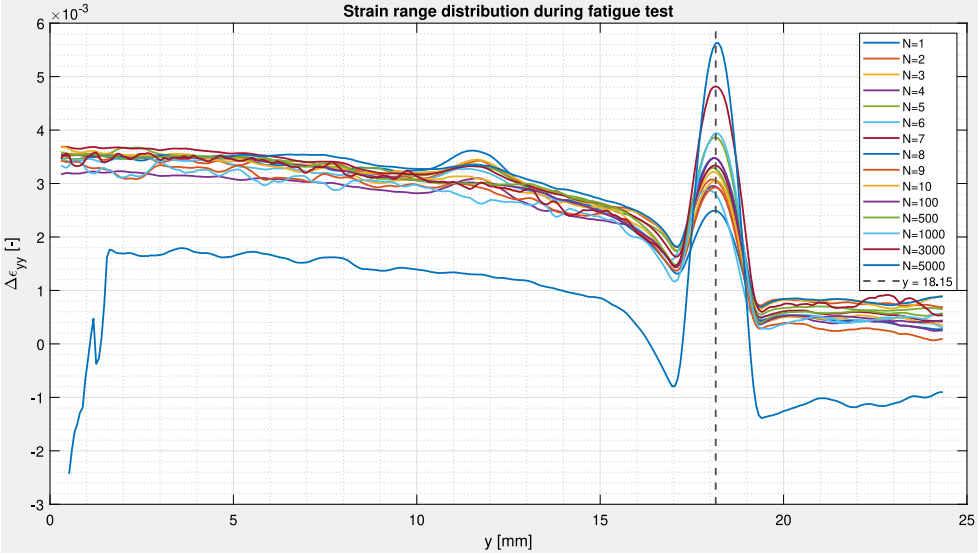

Fig. 21. Strain range distribution during the fatigue test along the loading axis y at the point $x = 5.03$ mm.

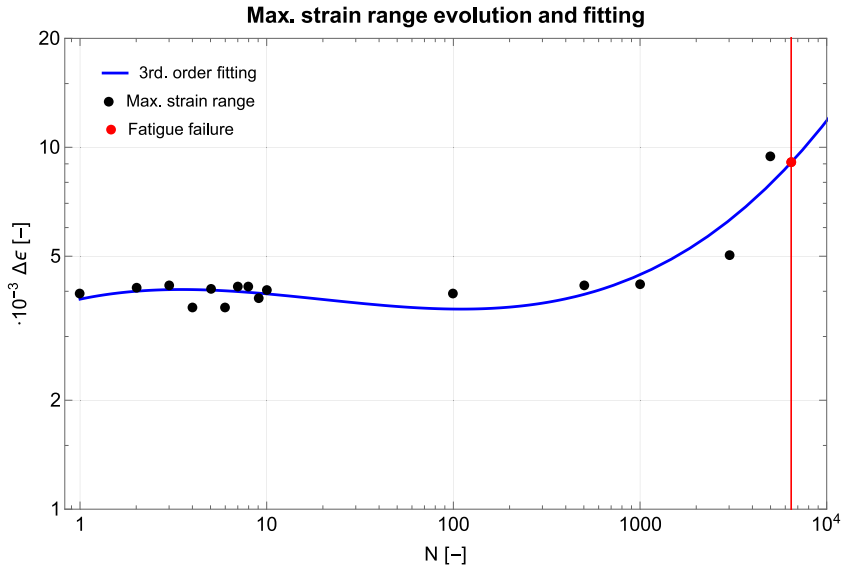

Fig. 22. Evolution of the maximum strain range during the fatigue test up to failure at $N = 6461$.

Table 7
Location and value of the maximum mean strain reached during the fatigue test up to failure at $N = 6461$.

N [−]	Mean Strain [−]	X-coord [mm]	Y-coord [mm]
1	0.0028106830	5.03	18.15
2	0.0037191529	4.96	18.15
3	0.0039716961	5.03	18.15
4	0.0043944288	5.11	18.07
5	0.0042340937	4.81	18.15
6	0.0045474143	5.03	18.07
7	0.0045519557	5.03	18.15
8	0.0045222252	5.11	18.07
9	0.0047032073	5.03	18.15
10	0.0044906849	5.03	18.15
100	0.0049210933	5.25	18.07
500	0.0051787668	5.03	18.15
1000	0.0057107847	5.03	18.15
3000	0.0063820897	5.33	18.07
5000	0.009800307	5.03	18.15
6461	0.0101393	–	–

Table 8
Mean strain evolution. Parameters of the fitting polynomial.

a_0	a_1	a_2	a_3
1.04785	0.406078	−0.1006	0.00806927

at the right of the bell the variation of the strain range is very small. Along the x axis, the mean strain does not vary much. Similar to the case of the strain range, at the loading cycle $N = 5000$ the mean strain range changes its behavior as well. At this moment, the mean strain increased notably along the loading axis y. This is particularly interesting since this cycle is close to the failure moment, which occurs at $N = 6461$.

Similar to the previous variables, the maximum mean strain can be also fitted by a third grade polynomial. The Table 8 shows the fitting parameters and Fig. 26 shows its fitting.

As it has been seen, in this case the mean strain distribution presents also a bell geometry on the TMAZ and its main peak is located in the same region where the maximum strain and strain range are reached.

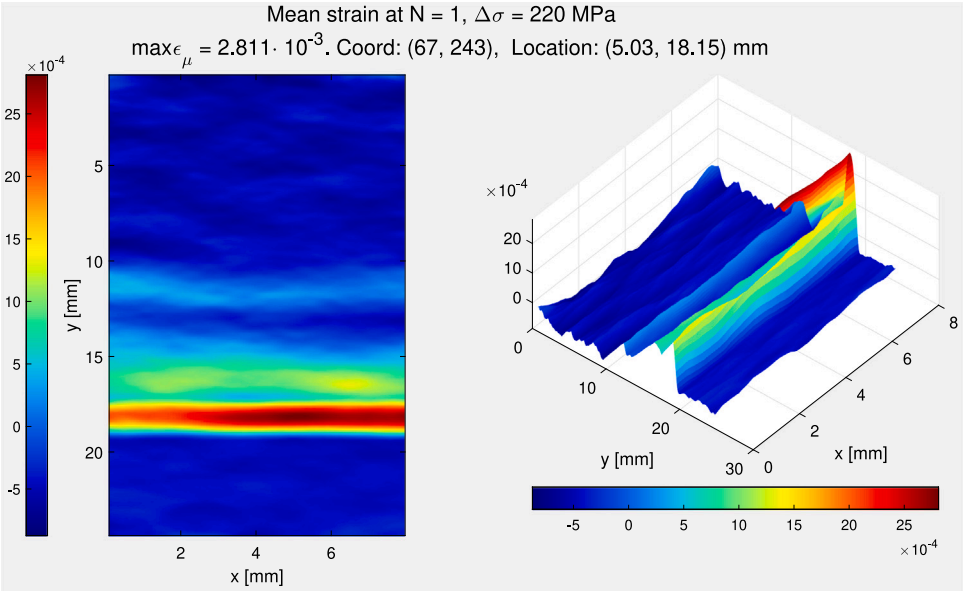

Fig. 23. Mean strain distribution at the loading cycle $N = 1$.

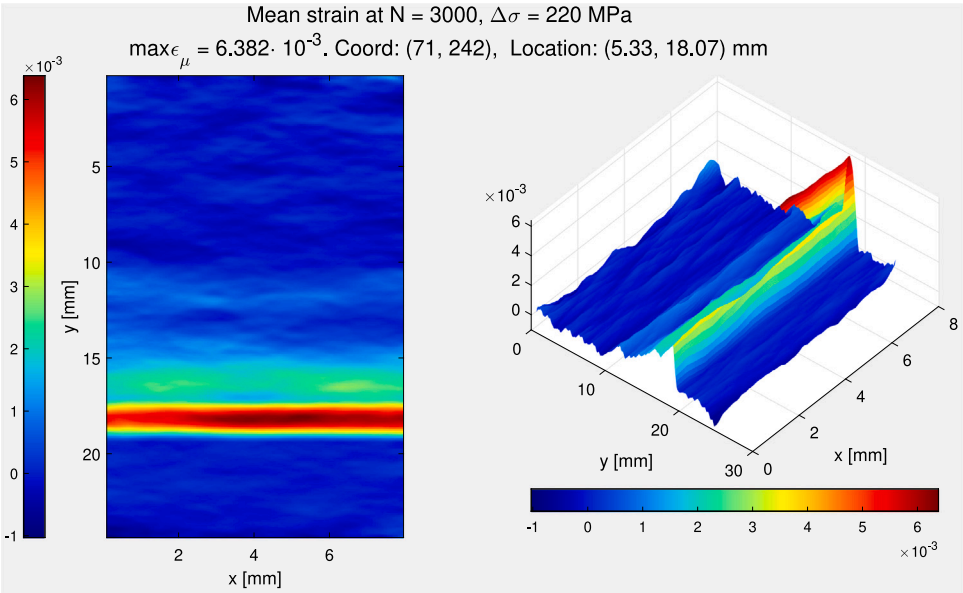

Fig. 24. Mean strain distribution at the loading cycle $N = 3000$.

Thus, this distribution and its evolution could be also modeled by applying the proposed methods.

4.6. Variation of the Smith-Watson-Topper (SWT) parameter during the fatigue experiment

In order to study the fatigue resistance during the fatigue test, the SWT parameter (Smith et al., 1970) given by

$$SWT = \sqrt{\frac{\Delta\epsilon}{2} \cdot \epsilon_{max}} \tag{5}$$

has been considered.

Usually, the SWT parameter is considered to study effect of mean strain on the fatigue strength and fatigue life in ULCF and LCF regimes. This fact is very important, since in the performed experiments, both strain range and mean strain change during loading cycles.

As expected the distribution of the SWT reaches its maximum values in the same region as the maximum and mean strain, see Table 9.

The Figs. 27 and 28 show the distribution of the SWT parameter during the loading cycle $N = 1$ and $N = 3000$. In the first loading cycle, the distribution presents two peaks with a bell geometry. However, as the tests continues, only one peak located around 18.5 mm on the loading axis y remains. This behavior is similar to those from the maximum and mean strain, so that, it can be also modeled by applying a Gaussian model.

The SWT distribution along the loading axis y shows also three peaks with a bell geometry at the points $y = 11.73, 16.08, 18.15$ mm, see Fig. 29. On the one hand, at the left of the bell the SWT parameter varies while the test continues. On the other hand, at the right of the bell the variation of the SWT parameter is very small. Along the x axis,it does not vary much. Similar to the case of the strain range, at the loading cycle $N = 5000$ the SWT parameter changes its behavior in a similar way. At this moment, which is close to fatigue failure, the SWT parameter decreased notably.

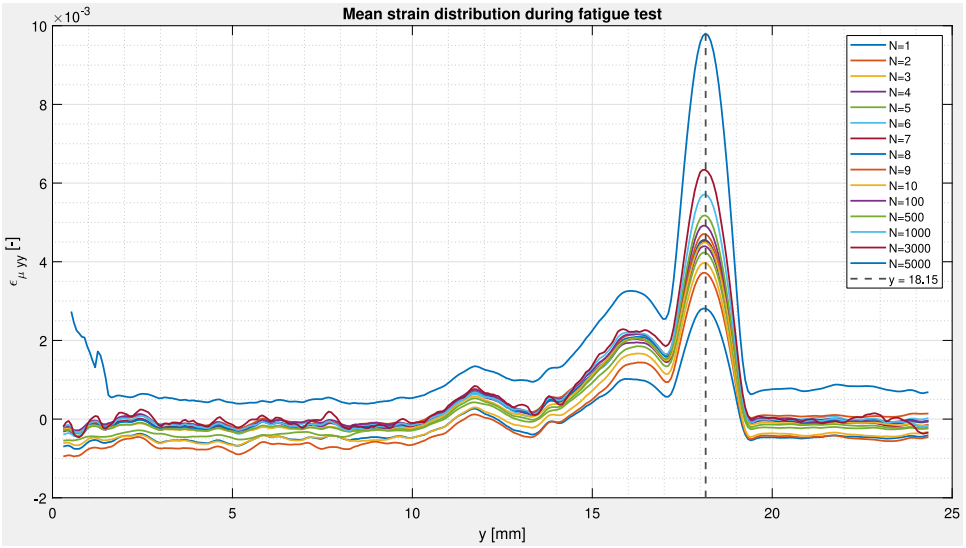

Fig. 25. Mean strain distribution during the fatigue test along the loading axis y at the point $x = 5.03$ mm.

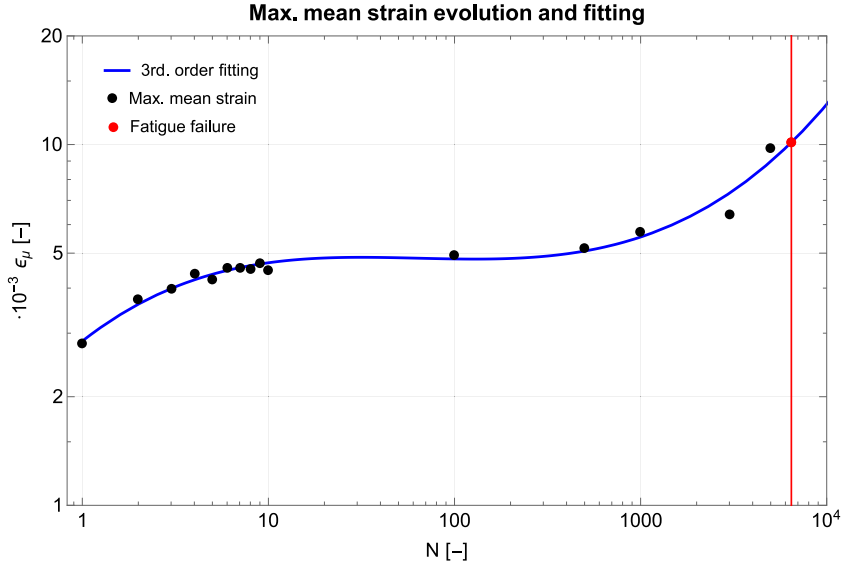

Fig. 26. Evolution of the maximum mean strain during the fatigue test up to failure at $N = 6461$.

Table 9
Location and value of the maximum PWM parameter reached during the fatigue test up to failure at $N = 6461$.

N [–]	SWT [–]	X coord [mm]	Y-coord [mm]
1	0.0023434783	7.93	18.15
2	0.0028824111	6.96	18.15
3	0.0030163693	4.81	18.07
4	0.0029575347	7.93	18.15
5	0.0031351284	6.89	18.15
6	0.0030404688	4.51	18.15
7	0.0032524011	7.93	18.15
8	0.0033041241	4.81	18.15
9	0.0030497558	7.93	18.15
10	0.0031090739	7.93	18.15
100	0.0034027956	4.81	18.15
500	0.0037193319	4.07	18.15
1000	0.0039581906	4.14	18.22
3000	0.0046296096	3.92	18.15
5000	0.006219029	7.93	18.22
6461	0.00649858	–	–

Table 10
SWT parameter evolution. Parameters of the fitting polynomial.

a_0	a_1	a_2	a_3
0.877137	0.240561	−0.0611828	0.00532087

Similar to the previous variables, the SWT parameter can be also fitted by a third grade polynomial. The Table 10 shows the fitting parameters and Fig. 30 shows its fitting.

The distribution of the SWT parameter presents also a bell geometry on the TMAZ and its main peak is located in the same region where the maximum strain and strain range are reached. Thus, this distribution and its evolution could be also modeled by applying the methods proposed in the previous sections.

5. Conclusions

As it has been seen, the DIC method offers a good alternative to model the strain, displacement and deformation during cyclic loading. Since the strain and its related variables play a fundamental role during

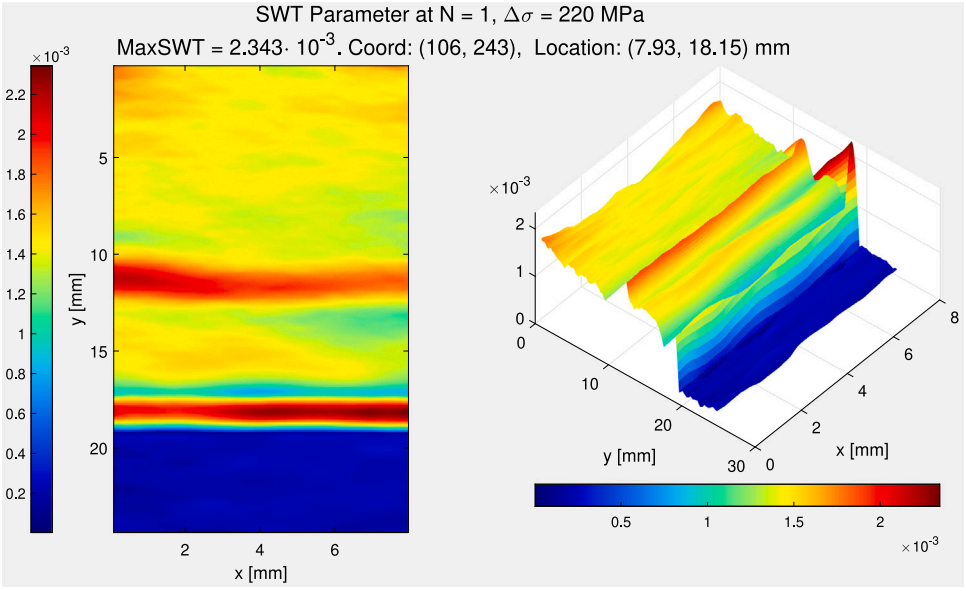

Fig. 27. SWT parameter distribution at the loading cycle $N = 1$.

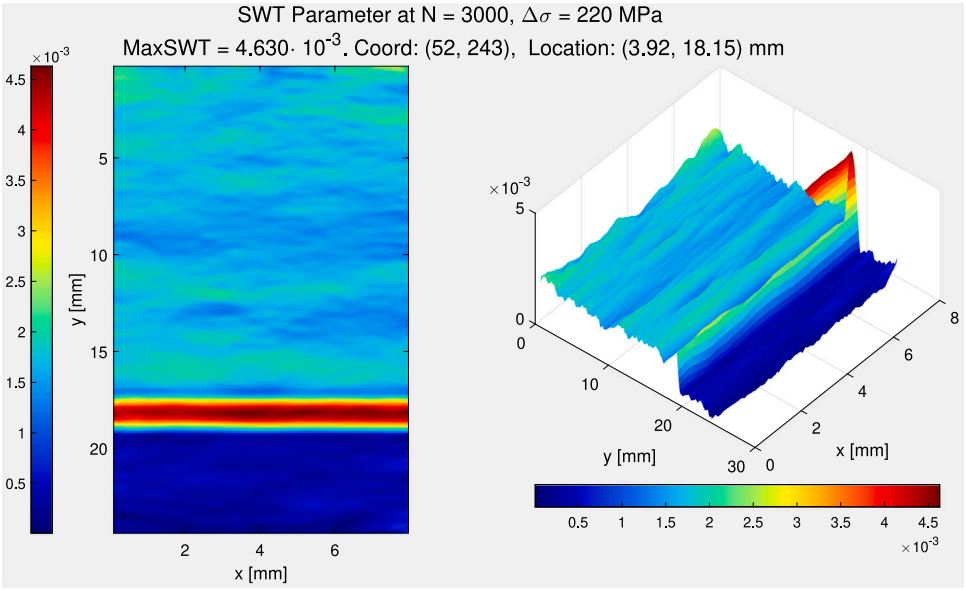

Fig. 28. SWT parameter distribution at the loading cycle $N = 3000$.

the fatigue in ULCF and LCF regimes, it seems reasonable to apply this method in order to estimate the fatigue strength of stir welded structures in these regimes.

In this study, the DIC method has offered interesting results regarding the distribution and evolution of four variables, the maximum reached strain, strain range, mean strain and SWT parameter.

Their distribution was evaluated at 15 loading cycles and the four variables show a symmetric bell geometry along the loading axis. The main peak of these bells was located in the region corresponding to the SZ. The fatigue failure was located along the interface between steel ans aluminum.

The evolution of these variables was modeled by third grade polynomial, which seems adequate to fit their corresponding data. The fitting polynomials show a similar behavior for all of the variables and allow to obtain a suitable estimation at the loading cycle where the fatigue failure occurs.

The obtained results suggest that modeling of the distribution and evolution of the strain and related variables can be a suitable approach to analysis the fatigue life of stir welded specimens.

However, despite the interesting results, it is necessary to perform subsequent fatigue tests by considering different stress ranges and ratios in order to estimate the fatigue life and to model $\Delta\epsilon - N$ the corresponding curves.

Declaration of competing interest

The authors declare that they have no known competing financial interests or personal relationships that could have appeared to influence the work reported in this paper.

Data availability

Data will be made available on request

Acknowledgments

The authors acknowledge support by the KIT-Publication Fund of the Karlsruhe Institute of Technology.

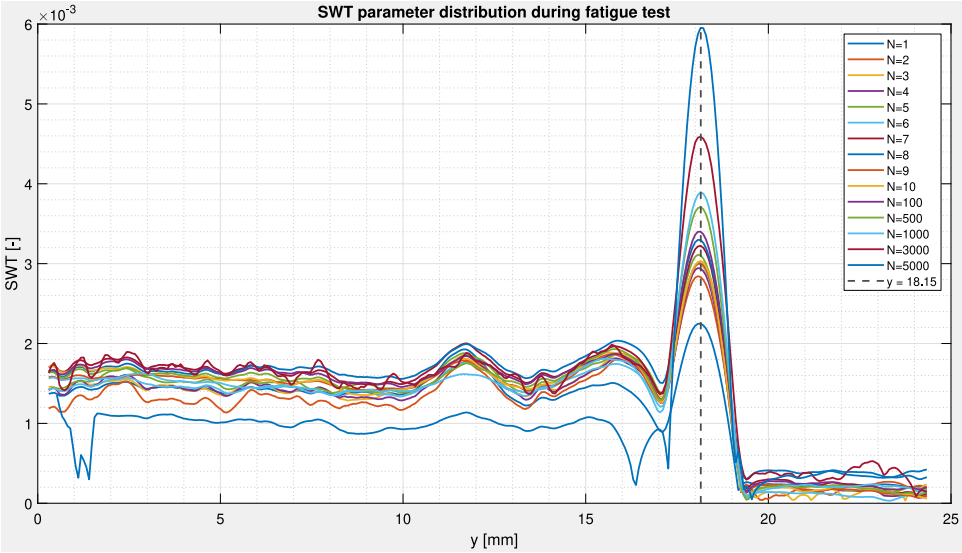

Fig. 29. SWT parameter distribution during the fatigue test along the loading axis y at the point $x = 5.03$ mm.

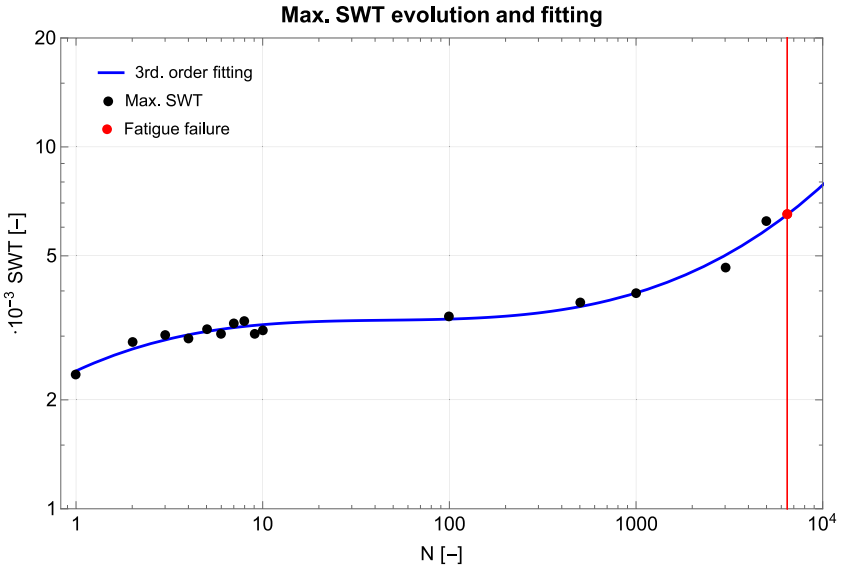

Fig. 30. Evolution of the maximum SWT parameter during the fatigue test up to failure at $N = 6461$.

References

Abdulqader, A., Rizos, D.C., 2020. Advantages of using digital image correlation techniques in uniaxial compression tests. Results Eng. 6, 100109. http://dx.doi.org/10.1016/j.rineng.2020.100109.

Chambers, D. (Ed.), 2017. Digital Image Correlation: Advanced Methods and Applications. In: Materials Science and Technologies, Nova Science Pub Inc.

Górszczyk, J., Malicki, K., Zych, T., 2019. Application of Digital Image Correlation (DIC) Method for Road Material Testing. Materials 12 (15), http://dx.doi.org/10.3390/ma12152349.

Hatano, R., Ogura, T., Matsuda, T., Sano, T., Hirose, A., 2018. Relationship between intermetallic compound layer thickness with deviation and interfacial strength for dissimilar joints of aluminum alloy and stainless steel. Mater. Sci. Eng. A 735, 361–366. http://dx.doi.org/10.1016/j.msea.2018.08.065, URL https://www.sciencedirect.com/science/article/pii/S0921509318311419.

Kumar, N., Yuan, W., Mishra, R.S., 2015. Friction Stir Welding of Dissimilar Alloys and Materials. Friction Stir Welding and Processing. Butterworth-Heinemann, http://dx.doi.org/10.1016/C2014-0-01707-8.

Liu, F., Dong, P., 2021. From thick intermetallic to nanoscale amorphous phase at Al-Fe joint interface: roles of friction stir welding conditions. Scr. Mater. 191, 167–172. http://dx.doi.org/10.1016/j.scriptamat.2020.09.031, URL https://www.sciencedirect.com/science/article/pii/S1359646220306308.

Matsuda, T., Hatano, R., Ogura, T., Suzuki, R., Shoji, H., Sano, T., Ohata, M., Hirose, A., 2020. Effect of mismatch in mechanical properties on interfacial strength of aluminum alloy/steel dissimilar joints. Mater. Sci. Eng. A 786, 139437. http://dx.doi.org/10.1016/j.msea.2020.139437, URL https://www.sciencedirect.com/science/article/pii/S0921509320305189.

Ogawa, D., Kakiuchi, T., Hashiba, K., Uematsu, Y., 2018. Mechanical properties of tailor welded Al/steel blanks made by friction stir welding and the effect of post heat treatment (in Japanese). Q. Jpn. Weld. Soc. 36 (3), 160–166.

Ogawa, D., Kakiuchi, T., Hashiba, K., Uematsu, Y., 2019. Residual stress measurement of Al/steel dissimilar friction stir weld. Sci. Technol. Weld. Join. 24 (8), 685–694. http://dx.doi.org/10.1080/13621718.2019.1588521.

Okane, M., Shitaka, T., Ishida, M., Chaki, T., Yasui, T., Fukumoto, M., 2017. Fatigue properties of butt welded aluminum alloy and carbon steel joints by friction stirring. In: 6th International Conference on Fracture Fatigue and Wear. In: Journal of Physics: Conference Series, vol. 843, IOPscience.

Sandnes, L., Welo, T., Grong, O., Berto, F., 2022. On the fatigue properties of a third generation aluminium-steel butt weld made by Hybrid Metal Extrusion & Bonding (HYB). Int. J. Fatigue 155, 106586. http://dx.doi.org/10.1016/j.ijfatigue.2021.106586, URL https://www.sciencedirect.com/science/article/pii/S0142112321004357.

Smith, K., Watson, P., H., T., 1970. A stress-strain function for the fatigue of metals. J. Mater. 5 (4), 767–778.

Uematsu, Y., Kakiuchi, T., Niimi, K., Toasa Caiza, P.D., 2021. Local strain analysis under quasi-static tensile loading in Al/steel dissimilar friction stir weld by a digital image correlation method. Int. J. Adv. Manuf. Technol. (in Press) 120, 349–360.

Uematsu, Y., Kakiuchi, T., Ogawa, D., Hashiba, K., 2020. Fatigue crack propagation near the interface between Al and steel in dissimilar Al/steel friction stir welds. Int. J. Fatigue 138, 105706. http://dx.doi.org/10.1016/j.ijfatigue.2020.105706, URL https://www.sciencedirect.com/science/article/pii/S0142112320302371.

Wang, T., Sidhar, H., Mishra, R.S., Hovanski, Y., Upadhyay, P., Carlson, B., 2019. Effect of hook characteristics on the fracture behaviour of dissimilar friction stir welded aluminium alloy and mild steel sheets. Sci. Technol. Weld. Join. 24 (2), 178–184. http://dx.doi.org/10.1080/13621718.2018.1503801.

Watanabe, T., Takayama, H., Yanagisawa, A., 2006. Joining of aluminum alloy to steel by friction stir welding. J. Mater Process. Technol. 178 (1), 342–349. http://dx.doi.org/10.1016/j.jmatprotec.2006.04.117.